Experimental investigation of deformation mechanisms during shear-enhanced compaction in poorly lithified sandstone and sand

Elin Skurtveit,[1,2,3] Anita Torabi,[1] Roy H. Gabrielsen,[4] and Mark D. Zoback[5]

Received 8 May 2013; revised 6 August 2013; accepted 8 August 2013; published 27 August 2013.

[1] Shear-enhanced compaction in shallow sandstone reservoirs has been investigated in laboratory experiments using high-pressure triaxial testing of poorly lithified sandstone and sand. We have studied the deformation mechanism involved during shear-enhanced compaction and controlling parameters for yield stress at varying confining pressures for sandstone/sand with different grain sizes, porosities, and packing. Experimental testing provides insights into the deformation mechanism during hydrostatic and axial compression of coarse- and fine-grained sands with different packing including (1) natural coarse-grained sandstone, (2) densely packed fine-grained sand, and (3) loosely packed fine-grained sand. Monitoring of deformation and ultrasonic velocity during deformation indicates porosity loss, compaction, and strain hardening for most of the samples. Visualization of deformation using pretest and posttest X-ray imaging and thin sections demonstrates localized deformation fabrics and grain damage. The results show grain rearrangement as the controlling deformation mechanism for material at low stress and high porosity, whereas for lower porosity and higher stress, grain fracturing controlled the deformation. The most pronounced localization of deformation was observed for the coarse-grained, low-porosity material. A Cam-Clay cap model was used to describe the porosity loss during compaction and shear-enhanced compaction, demonstrating large inelastic compaction with increasing confining pressure. Yield stress and end caps for poorly lithified sandstone are observed for various porosities and stress conditions and found to be lower than predicted using empirical relationships for sandstone.

Citation: Skurtveit, E., A. Torabi, R. H. Gabrielsen, and M. D. Zoback (2013), Experimental investigation of deformation mechanisms during shear-enhanced compaction in poorly lithified sandstone and sand, *J. Geophys. Res. Solid Earth*, *118*, 4083–4100, doi:10.1002/jgrb.50342.

1. Introduction

[2] Shallow saline aquifers and depleted petroleum reservoirs are suggested as promising reservoirs for geological storage of CO_2, and in order to fulfill safe storage criteria, knowledge about deformation mechanisms in poorly lithified sandstone is essential. Successful CO_2 injection requires high-quality reservoirs. The compositions of reservoirs and the properties, geometry, and distribution of structures related to faults play a major role for fluids [*Eichhubl et al.*, 2004; *Fisher and Knipe*, 2001] and for understanding fault reactivation due to changes in reservoir stress conditions [*Cuisiat et al.*, 2010]. Localized deformation in the form of deformation bands can be observed in many porous sandstone reservoirs [*Fossen et al.*, 2007]. The microfabric produced within deformation bands is controlled by the deformation mechanisms, which in turn are governed by external conditions such as the state of stress and burial depth (pressure and temperature) as well as lithological and petrophysical properties [*Cheung et al.*, 2012; *Soliva et al.*, 2013]. Hence, in order to understand the role of deformation bands in deformation of porous sandstone and sand, a better understanding of deformation mechanism and stress conditions during deformation of poorly lithified and noncemented sands is needed.

[3] Deformation structures described for sandstone reservoirs have been focused on deformation bands observed in well-lithified sandstones that have experienced considerable burial and subsequent uplift, such as the Entrada, Navajo, and Aztec Sandstones [*Antonellini et al.*, 1994; *Eichhubl et al.*, 2004; *Solum et al.*, 2010; *Sternlof et al.*, 2004]; the Arran New Red Sandstone [*Underhill and Woodcock*, 1987]; the Nubian Sandstone [*Du Bernard et al.*, 2002]; and the Brumunddal Sandstone [*Lothe et al.*, 2002]. However, the time of formation of bands is often suggested

[1]Centre for Integrated Petroleum Research, Bergen, Norway.
[2]Earth Science Department, University of Bergen, Bergen, Norway.
[3]Norwegian Geotechnical Institute, Oslo, Norway.
[4]Department of Geoscience, University of Oslo, Oslo, Norway.
[5]Department of Geophysics, Stanford University, Stanford, California, USA.

Corresponding author: E. Skurtveit, Norwegian Geotechnical Institute, Sognsveien 72, NO-0855 Oslo, Norway. (esk@ngi.no)

2169-9313/13/10.1002/jgrb.50342

to be at shallow burial conditions [*Fossen*, 2010; *Schultz*, 2009]. There are also examples of cataclastic deformation bands observed in poorly lithified sandstone, demonstrating that grain crushing can occur even at shallow burial depths in such bands [*Ballas et al*., 2012; *Balsamo and Storti*, 2010, 2011; *Cashman and Cashman*, 2000; *Skurtveit et al*., 2012; *Torabi*, 2012]. Based on field observation of various types of deformation bands, several important characteristics can be noted [*Antonellini et al*., 1994; *Aydin et al*., 2006; *Eichhubl et al*., 2010; *Fossen et al*., 2007]: (1) a large variation in grain-scale deformation ranges from no grain damage to grain crushing; (2) the deformation mode can be dilation, shear, or compaction; and (3) shear along the band can vary from no shear displacement to a well-developed slip surface. Shear-enhanced compaction bands are planar and typically composed of multiple parallel strands with an angle relative to the maximum compressive principal stress [*Ballas et al*., 2013; *Eichhubl et al*., 2010], whereas pure compaction bands are typically wavy or chevron in geometry and form close to perpendicular to the maximum compressive principal stress [*Eichhubl et al*., 2010]. The modes of compaction localization are described as discrete or diffuse bands based on their thickness [*Baud et al*., 2004; *Wong and Baud*, 2012], or the compaction can be distributed.

[4] Factors controlling the large variation in textural composition, mode of deformation, and shear displacement can be investigated using laboratory experiments using different experimental setups, loading conditions, and materials. Localization of shear deformation in sand is well studied in geotechnical labs using a variety of grain size, angularity, sorting, and sample density of the studied sands. Most of these tests are performed at low consolidation pressure (up to 1 MPa), forming localized shear bands dominated by dilation and with little evidence of grain damage in plane strain and triaxial tests [*Desrues and Viggiani*, 2004; *Hall et al*., 2010]. Furthermore, confining pressures up to 8 MPa in extensional plane strain experiments show deformation with no grain crushing [*Rykkelid and Skurtveit*, 2008]. Experimental work that reports grain damage and formation of cataclastic bands is mainly from triaxial tests on well-lithified (cemented) sandstone [*Baud et al*., 2004; *Bésuelle et al*., 2000; *Fortin et al*., 2005; *Lothe et al*., 2002; *Mair et al*., 2000; *Olsson*, 1999; *Zhang et al*., 1990a]. The transition in deformation mode from shear to compaction is also well studied for well-lithified and cemented sandstone [*Baud et al*., 2004; *Eichhubl et al*., 2010; *Fortin et al*., 2005; *Tembe et al*., 2008], and an interesting finding is that considerably higher pressures are required for the experimental formation of compaction bands than those suggested from field observations [*Eichhubl et al*., 2010; *Schultz*, 2009].

[5] Experimental work focusing on the deformation mechanism in uncemented and poorly lithified sandstone typical for shallow reservoir conditions is limited. High-pressure testing of compaction of sand shows that the yield strength relates to onset of grain crushing and varies largely with sand properties [*Chuhan et al*., 2003; *Mesri and Vardhanabhuti*, 2009]. Triaxial compression testing of Ottawa sand at high pressure is associated with considerable grain crushing and permeability anisotropy [*Zoback and Byerlee*, 1976]. Significant grain failure is also observed in experiments on loose sand by *Karner et al*. [2003] using acoustic emission rates for quantification. Similar experiments at elevated temperature are used to discuss the hydrothermal effect on the yield behavior of sand [*Karner et al*., 2008]. The formation of cataclastic deformation bands in sand is observed in experiments using a special high-pressure ring shear device [*Cuisiat and Skurtveit*, 2010; *Torabi et al*., 2007] where grain crushing is observed for shear bands that formed at vertical stress corresponding to a 500 m burial depth or more [*Cuisiat and Skurtveit*, 2010], and the amount of grain damage is found to increase with increasing vertical stress and shear displacement [*Torabi et al*., 2007]. In a ring shear device, shearing is imposed on a predefined zone between the confining rings. However, to investigate the localization of strain in different deformation modes and changes in deformation band angles during localization, an axial symmetrical triaxal test setup is used [*Fortin et al*., 2005; *Wong and Baud*, 2012; *Wong et al*., 1997].

[6] In the present work, a novel study of deformation mechanism and conditions for shear-enhanced compaction is investigated for poorly lithified sandstone and sand using high-pressure triaxial testing. A series of triaxial tests consisting of one hydrostatic test and two to three axial compression tests at various confining pressures was performed for coarse- and fine-grained sands with different packing including (1) natural coarse sandstone, (2) densely packed fine sand, and (3) loosely packed fine sand. Axial and radial deformation together with monitoring of ultrasonic velocity was used to identify variations in porosity loss and shear-enhanced compaction during deformation. Posttest X-ray computed tomography (CT) imaging together with pretest X-ray imaging of some tests is used for visualization of deformation localization, while thin sections are used for microstructural study of grain damage in the final samples. A Cam-Clay cap model [*Schultz and Siddharthan*, 2005] was used to describe the porosity loss during compaction and shear-enhanced compaction for the studied materials, demonstrating the large inelastic compaction observed for these materials and to show how the deformation mode and mechanisms vary with confining pressures for the different samples.

2. Application of a Modified Cam-Clay Cap Model for Porous Sandstone

[7] The kinematical varieties of deformation bands, i.e., dilation, shear, and compaction bands, localize inelastic deformation that can be described by a modified Cam-Clay cap model [*Schultz and Siddharthan*, 2005]. The theoretical framework for these modified Cam-Clay cap models is based on models developed for soil mechanics, describing the transition from elastic to plastic deformation [*Bésuelle and Rudnicki*, 2003], and further was adopted to deformation bands observed in sandstone reservoirs [*Aydin and Johnson*, 1983; *Rudnicki and Rice*, 1975]. Hence, the Cam-Clay cap models are used for understanding the deformation mechanism involved in various types of deformation bands observed in the field [*Wibberley et al*., 2007] and to increase our knowledge about deformation mechanisms in these structures.

[8] The modified Cam-Clay cap elastoplastic model (Figure 1) is described using the differential stress, $q = \sigma_1 - \sigma_3$, and mean effective stress, $p' = (\sigma_1 + 2\sigma_3)/3 - p_p$, where σ_1 and σ_3 are the vertical applied stress and the confining stress, respectively, and P_p is the pore pressure.

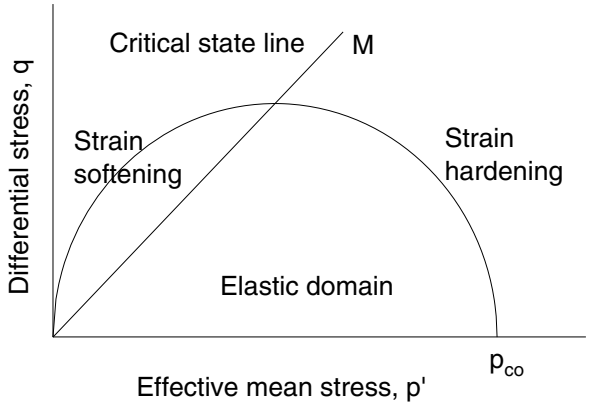

Figure 1. Elliptical yield cap for the modified Cam-Clay cap model.

In the $p-q$ space, the yield surface is described using an ellipse centered on the p' axis and passing through the origin in the effective stress space. The yield function f defines the elastic-plastic boundary for a symmetrical yield surface given by

$$f\{p',q,p_{co}\} = q^2 + M^2 p'(p' - p_{co}) \quad (1)$$

[9] The equation describes an ellipse with a shape controlled by M and the size controlled by p_{co}, where p_{co} defines the elastic limit or yield stress along a hydrostatic loading path. This parameter is sometimes referred to as the preconsolidation pressure or "memory" of the material [*Crawford et al*., 2004], whereas *Wong et al*. [1997] related this parameter to the grain-crushing pressure, P^*. The shape parameter M defines a line where the material deforms in a strictly frictional manner, with no compaction or dilation, named the critical state line [*Schultz and Siddharthan*, 2005]. The critical state line M for a material is given by

$$M = (6\sin\varphi)/(3 - \sin\varphi) \quad (2)$$

where φ is the Mohr-Coulomb friction angle for residual sliding. The critical state line defines an area to the left where the material yields with dilation and experiences softening, whereas to the right, the material yields in compaction and experiences strain hardening (Figure 1).

[10] The transition from brittle faulting to cataclastic flow in porous sandstone was investigated using triaxial compression experiments with a broad range of effective pressures [*Baud et al*., 2004; *Fortin et al*., 2005; *Wong and Baud*, 2012; *Wong et al*., 1997]. These experimental data were used to identify initiation of shear-enhanced dilation in the brittle regime and shear-enhanced compaction that results from cataclastic flow at high effective pressure. The results of the experiments were modeled utilizing the elliptical yield envelope comprising shear yield surface and cap. The size of the yield cap was found to be controlled by the elastic limit or yield stress, P_{co}, as seen along a hydrostatic loading path. This yield stress has been related to the porosity and grain size of sandstone [*Wong et al*., 1997] and named P^*, whereas for noncemented sand, the yield stress can also be related to the preconsolidation pressure of the material tested [*Crawford et al*., 2004]. Preconsolidation pressure can be linked to the maximum burial depth experienced by the material or preconsolidation used during mechanical testing.

3. Material Used for Testing

[11] In the current test program, we used two noncemented, shallowly buried sandstones, sampled in the Uchaux sands at the Boncavaï quarry (Southeast Basin, Provence, France). These Turonian deltaic to beach sands are about 120 m thick and show a large range of grain size and porosity. They are mainly composed of quartz (95%–96.5%) with some feldspar (3%–4.5%) and few fragments of clay (0.5%) [*Ballas et al*., 2013]. The deformation structures observed in these localities include cataclastic shear bands and larger ultracataclastic faults sometimes including discrete slip surfaces [*Ballas et al*., 2012; *Wibberley et al*., 2007]. Shear-enhanced compaction bands are also described in certain sand layers within this sand-dominated unit [*Ballas et al*., 2013]. An overall lack of diagenetic features observed in the formations, together with regional stratigraphic considerations, suggests that the maximum burial was

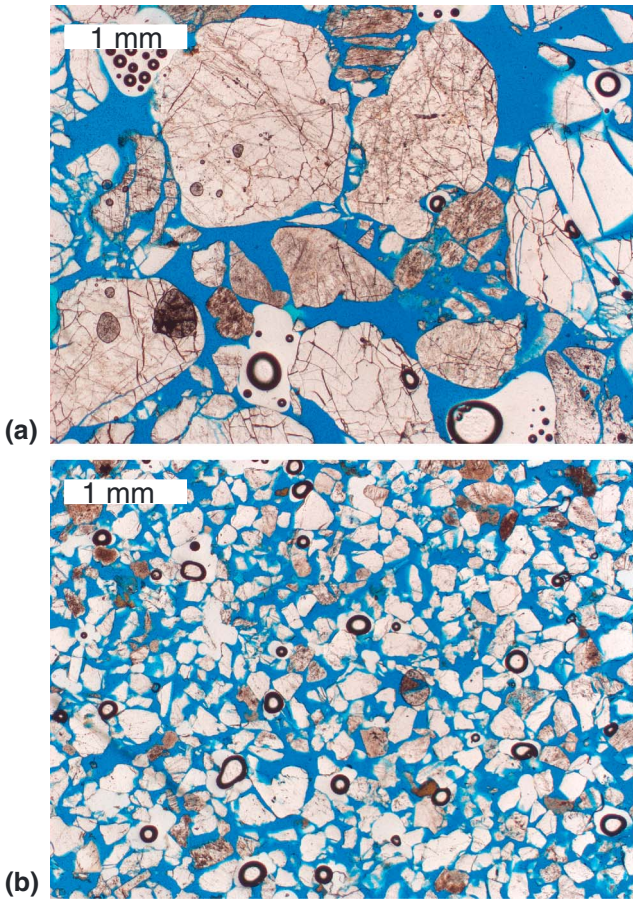

Figure 2. Photomicrograph of the sands used in this study showing grain size and fractured grains in the sample before testing in the laboratory. (a) Coarse-grained natural sandstone material and (b) fine-grained natural sandstone material. Black rings are trapped air or water before the epoxy impregnation. Note a better sorting in the fine-grained sand.

Table 1. Grain Size, Sorting, and Unit Weight for Disintegrated Sands From the Boncavai Quarry

	Grain Size	Sorting	Unit Weight of Grains
	d50	d60/d10	Υ_g
Sand	(mm)		(kN/m^3)
Coarse	0.65	4.1	25.84
Fine	0.2	1.7	25.89

relatively shallow (around 400 m) [*Ballas et al*., 2013]. The materials tested in this work were a coarse-grained sandstone with an in situ porosity of around 27% and a more fine-grained sandstone with an in situ porosity of around 37% [*Ballas et al*., 2013].

[12] The sands used for the present tests are characterized by the grain size distribution and sorting. Grain size was determined using standard sieving analyses on disintegrated sand. Mean grain size is represented by the diameter at 50% passing, d50, whereas sorting is given as the uniformity coefficient, d60/d10. The coarse sand (Figure 2a) has a mean grain size of 0.65 mm and a uniformity coefficient of 4.1, whereas the fine sand (Figure 2b) has a mean grain size of 0.2 mm and a uniformity coefficient of 1.7 which means that the fine sand is better sorted than the coarse-grained sand (Table 1). Qualitative comparison of the two different sands indicates a similar grain shape. The porosity of the tested sands is higher than the in situ porosity given by *Ballas et al*. [2013] due to the sample preparation and possible natural variations within the formation.

4. Sample Preparation

[13] Two different sample preparation methods were applied in the test program, namely, coring of frozen intact blocks and tamping of sand from disintegrated sandstone.

4.1. Coring of Plugs From Frozen Block

[14] A set of plugs was cored from a single block from the coarse-grained Uchaux sands. Because of poor lithification, the block sample was saturated with water and frozen before plugs were drilled, using a glycol with a temperature of −12°C as drilling fluid. All plugs were drilled with a horizontal orientation, and each plug had an approximate diameter of 38 mm and a height of 65–76 mm. The plugs were kept frozen until mounted inside the nitril rubber sleeve used in the triaxial cell. For the hydrostatic test, the plug was mounted into the triaxial cell in frozen condition, whereas for the axial compression tests, the plugs were put into the sleeve in a frozen condition and were then thawed before being imaged using an X-ray computed tomography (CT) scanner. After the scanning, the plug was mounted in the triaxial cell and vacuum was applied.

4.2. Tamping of Sand Using Undercompaction

[15] The poorly lithified Uchaux sands easily disintegrated, allowing the usage of conventional geotechnical methods for testing sand. Triaxial sand samples prepared from the fine-grained sand were tamped into the sleeve in the triaxial setup using the undercompaction method described by *Ladd* [1978]. The sleeve was mounted onto a 38 mm triaxial pedestal using a split mold to keep the sleeve in position during tamping. The sand was tamped into the sleeve in a moist condition in six layers with a total height of 80 mm. In layer numbers 3, 4, and 5, a small amount of iron was mixed with the sand in a thin zone at the bottom of the layer to make a marker horizon that was visible in the X-ray images. The weight of sand used in each layer was applied to calculate the sample density and porosity. When the sample was tamped to the given height with filter disks in both ends, the sleeve was sealed off and vacuum was applied before removal of the split ring. The tamped samples were imaged using X-ray CT scanning after the test.

5. Experimental Device and Methods

[16] Triaxial tests were performed using equipment located at the Norwegian Geotechnical Institute. Details about the equipment and practice for triaxial testing methods applied are given in *Berre* [2011]. The horizontal strain of the specimen was measured by two horizontal strain sensors. Each sensor consists of a submersible linear variable differential transformer (LVDT) fixed in a very light metal ring, which encloses the specimen. One horizontal strain sensor was used in measuring the change in the diameter at the lower third point of the specimen, and one was used to measure the change in the diameter at the upper third point. The two diameters were oriented 90° apart. The internal local measurement of the vertical strain was obtained by recording the change in distance between the two horizontal strain sensors using two LVDT sensors. Volumetric strain was calculated both from the deformation measurements and from expelled pore fluid. All-around confining pressure was applied to the specimen through oil pressure in the main pressure chamber. The axial compression was transferred by a loading press.

[17] The transit time for ultrasonic compressional waves was measured in the axial direction using piezoelectric transducers pulsing sinusoidal waves with a frequency of 0.5 MHz. The transducers were placed within the top and bottom pedestal. Corrections for travel time within the pedestal and filters were performed during data processing using head-head measurements. Compressional velocities (Vp) were computed from measured transit time and sample dimensions. Uncertainties in the velocity measurements can be estimated using the analysis described by *Wang and Gelius* [2010] and *Mondol et al*. [2008], where the errors in

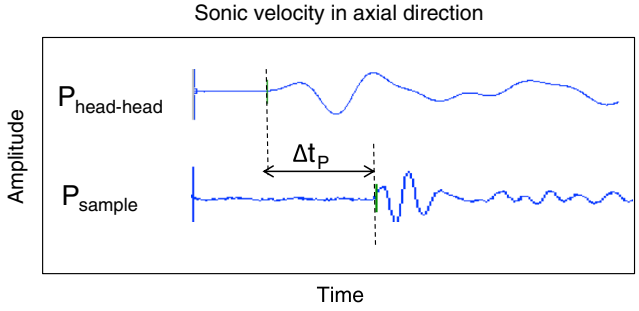

Figure 3. Example of *P* wave signal for head-to-head measurement and for the sample. The time Δt_p is the travel time in the sample.

Table 2. Material, Pressure Conditions, and Porosity for Each Test Within the Test Program

Material	Packing Density	Hydrostatic Loading Pressure (MPa)	Axial Compression	Initial Porosity (%)	Porosity at Start Loading (%)	Posttest Thin Sections	CT Scans
Natural coarse sandstone	Natural	40		36.56	35.91	-	Posttest
		2	Yes	35.23	34.59	-	Pretest and posttest
		5	Yes	38.16	37.11	Yes	Pretest and posttest
		15	Yes	35.06	34.28	Yes	Pretest and posttest
Fine sand	Loose	40		45.62	45.21	Yes	Posttest
		2	Yes	46.00	45.47	Yes	Posttest
		5	Yes	46.26	45.74	Yes	Posttest
Fine sand	Dense[a]	40		41.22	41.07	Yes	Posttest
		2	Yes	39.78	39.75	Yes	Posttest
		5	Yes	40.84	40.68	Yes	Posttest
		15	Yes	40.98	40.81	Yes	Posttest

[a]A thinner membrane has been used for the four tests on dense sand.

picks and sample height are considered. Considering a precision of the LVDT for a sample height of ±0.2 mm and a precision in arrival time picking of 0.5 µs, the error for a *P* wave velocity of 2000 m/s is found to be ±2.5%. An example of head-to-head arrival and *P* wave arrival time is shown in Figure 3. A Nikon Metrology industrial high-resolution 3-D computed tomography (CT) scanner equipped with a 225 kV microfocus X-ray tube is used for imaging the material before and after testing. The voxel resolution during the scans was 26.1 µm. Three-dimensional images were reconstructed on a powerful 64 bit computer using VGStudio MAX by Visual Graphics.

[18] The experimental procedure used in this study is based on recommendations for triaxial testing of soft rock as described in *Berre* [2011] and methods used previously for defining the cap and the transition between compaction and shear failure in triaxial tests on cemented sandstone [*Baud et al.*, 2004; *Fortin et al.*, 2005; *Wong et al.*, 1997]. A similar approach was used for triaxial testing of uncemented poorly lithified sandstone and sand. The aim was to study the variation in deformation mode and grain damage during shear-enhanced compaction at various burial depths and material properties using stress conditions representative for shallow burial depth.

[19] The experimental test procedure is divided into two main phases: one hydrostatic loading phase where the material was isotropically loaded to a given consolidation stress, followed by an axial compression phase. During each experiment, a confining pressure of 0.5 MPa was applied to the sample and vacuum was replaced with de-aerated tap water for saturation. For the plugs drilled from frozen samples, one to two pore volumes with water were circulated through each sample with water at atmospheric pressure to replace any glycol left from the drilling. The tamped samples rested for some minutes to reach full saturation. The pore pressure and confining stress were then raised simultaneously to 1 and 1.5 MPa, respectively. All the tests were performed under drained conditions, using a back pressure of 1 MPa and cell pressure increased to the target confining pressure using a rate of 2 MPa per h. The hydrostatic tests were loaded isotropically to 40 MPa mean effective pressure, whereas the tests combined with shearing were loaded isotropically to 2, 5, and 15 MPa mean effective pressures before axial compression at a rate of 10–6 s^{-1}. The duration of each test

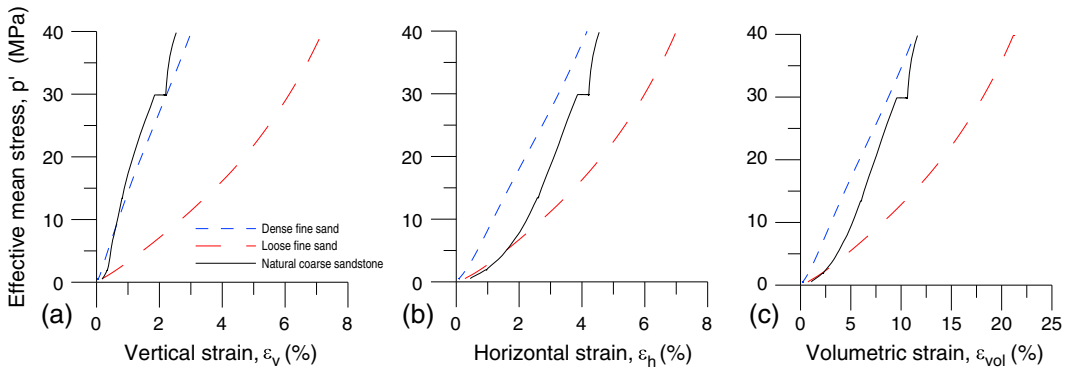

Figure 4. Mean stress as a function of (a) vertical strain, (b) horizontal strain, and (c) volumetric strain during isotropic loading up to 40 MPa for the tree types of material tested. Color codes for curves are given in the inset legend. The kink in the curve for the natural coarse-grained sandstone is due to a pause in loading at 30 MPa mean effective stress.

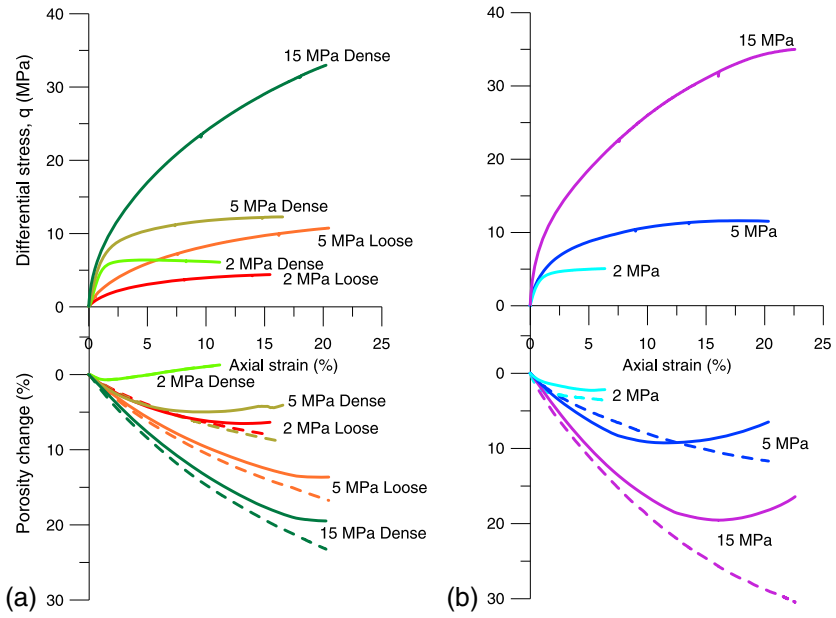

Figure 5. Mechanical data from the triaxial tests on (a) loose and dense fine sand and (b) intact coarse sandstone. Differential stress and porosity are plotted against axial strain. Positive porosity change is compaction, whereas reduction is dilation. The solid lines represent deformation and porosity from internal LVDT strain measurements, whereas the dashed lines represent porosity change calculated from expelled pore fluid.

was around 2–4 days. Pressure conditions, initial packing, porosity, and visualization techniques used for each test in the program are given in Table 2.

[20] Axial compression was stopped at around 20% volumetric strain or when the internal horizontal strain sensors went out of range. At the end of the test, the pore pressure valve was closed and the sample was unloaded, creating a vacuum in the sample. During dismounting, the plug was kept inside the rubber sleeve and then it was moved to the X-ray CT scanner. For the coarse natural sandstone material, the vacuum was released before moving the sample to the X-ray CT scanner, whereas for the fine sand, vacuum was maintained during scanning. After scanning, the sample was gently pushed out of the membrane and dried, and intact parts of the sample were impregnated with blue epoxy for thin section purposes. After drying the sample, the exact weight of dry material of the intact samples was determined.

6. Experimental Results

6.1. Mechanical Data

[21] For the three main types of materials, an isotropic/hydrostatic loading test was performed in each case to establish the compaction properties of the material and as a

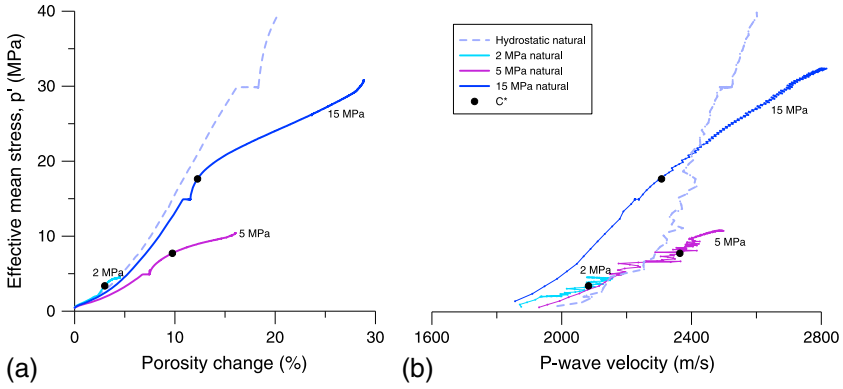

Figure 6. Natural coarse-grained sandstone: the (a) effective mean stress versus porosity change and (b) effective mean stress versus *P* wave velocity for hydrostatic loading up to 40 MPa and axial compression at 2, 5, and 15 MPa confining pressures. Positive porosity change is reduction in porosity. Interpreted onset of yield due to shear-enhanced compaction, C*, is marked on the curves. The kink in the hydrostatic loading curve is due to a pause in loading at 30 MPa mean effective stress.

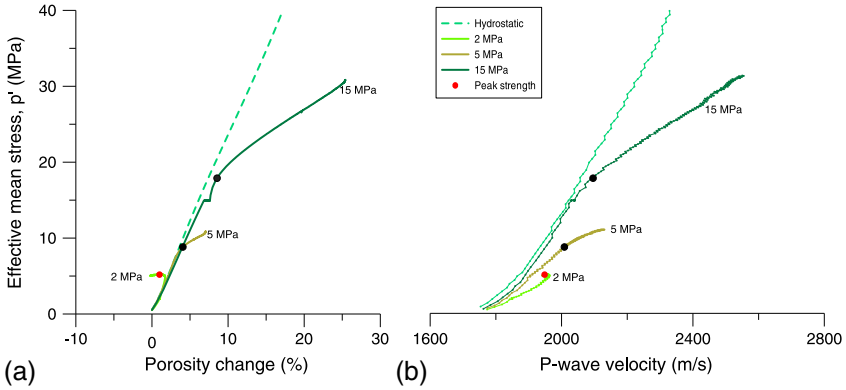

Figure 7. Mean stress as a function of porosity and *P* wave velocity changes for a fine-grained dense sand: the (a) effective mean stress versus porosity change and (b) effective mean stress versus *P* wave velocity are shown for hydrostatic loading up to 40 MPa and axial compression at 2, 5, and 15 MPa confining pressures. Positive porosity change is reduction in porosity. Interpreted onset of yield due to shear-enhanced compaction, C*, and peak stress are marked on the curves.

reference for the axial compression loading stage (Figure 4). The hydrostatic loading shows that the natural coarse-grained sandstone sample and the dense, fine-grained sand had a comparable stiffness, whereas the loose fine-grained sand is less stiff and suffered considerable deformation. The shape of the isotropic loading curve is similar in the horizontal and vertical orientations for the two sands tampered into the sleeve, whereas for the natural, coarse-grained sandstone, the material seems to be stiffer in the vertical as compared to the horizontal direction. This could possibly be related to an unevenness of the drilled plug surface, and this should be kept in mind when using the porosity data from the tests on the natural sandstone samples. The pause in loading at 30 MPa for the intact coarse material shows that there is considerable secondary deformation (creep) in the material.

[22] Axial compression loading was applied at 2, 5, and 15 MPa confining pressures for the natural coarse-grained sandstone and the dense fine-grained sand, whereas the loose fine-grained sand was loaded at 2 and 5 MPa confining pressures. The stress-strain behavior and volumetric changes during axial compression for the fine and the coarse material are compared by plotting the differential stress and porosity versus axial strain in Figure 5. The porosity was calculated using the volumetric strain data from both the local strain measurements and expelled pore fluid. The stress-strain curve (Figures 5a and 5b) can be divided into three stages: (1) an initial loading phase seen as a linear change in the stress-strain curve, (2) a nonlinear change of the stress-strain curve, and (3) a last phase of axial deformation at nearly constant differential stress with the exception of tests at 15 MPa. The three stages of deformation are most pronounced for the natural coarse-grained sandstone and the dense fine-grained sand at low confining stresses of 2 and 5 MPa, whereas the loosely packed fine-grained sand is dominated by nonlinear deformation. Maximum differential stress reached during the tests appears to be controlled by the confining stress during axial loading rather than the material, whereas the material and initial packing influences the shape of the stress-strain curve and the onset of shear-enhanced compaction.

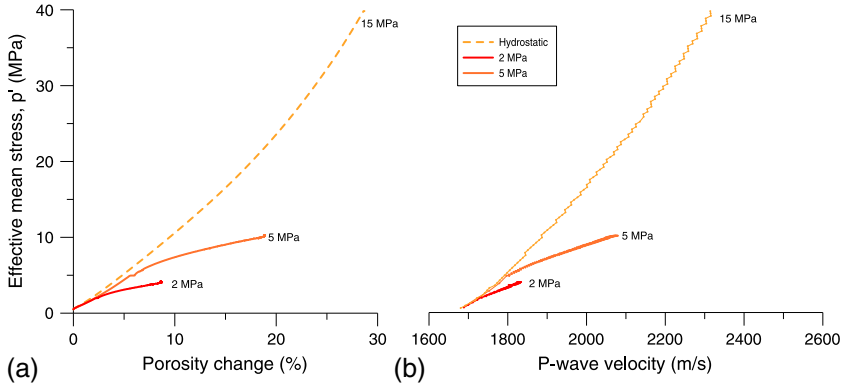

Figure 8. Mean stress as a function of porosity and *P* wave velocity changes for a fine-grained loosely packed sand: the (a) effective mean stress versus porosity change and (b) effective mean stress versus *P* wave velocity for hydrostatic loading up to 40 MPa and axial compression at 2 and 5 MPa confining pressures. Positive porosity change is reduction in porosity. Onset of yield due to shear-enhanced compaction is not interpreted for this test.

Table 3. Stress Conditions at Onset of Shear-Enhanced Compaction, C*, and the Maximum Stress Conditions for Tests With Axial Loading

		Onset of Shear-Enhanced Compaction		Maximum Stress	
	Hydrostatic Consolidation	p'	q	p'	q
Material	(MPa)	(MPa)	(MPa)	(MPa)	(MPa)
Natural coarse sandstone	2	3.4	2.8	4.5	5
	5	7.7	5.6	10	10
	15	17.7	5.5	17	34
Dense fine sand	2	-	-	5.1	6.3
	5	8.8	7.7	11	12
	15	17.9	5.8	30	31
Loose fine sand	2	-	-	4.1	4.4
	5	-	-	10	10.2

[23] The porosity change associated with the tests on both fine- and coarse-grained materials (Figures 5a and 5b) shows that the largest porosity decrease occurred in the initial stage of the test, followed by a more gradual decrease. Porosity determined from local strain measurements and expelled pore fluid shows a similar trend in the incipient stages of the tests. By increasing axial strain, the local strain values generally show a lower decrease in porosity than that determined from the expelled pore fluid. This is most pronounced for the natural coarse-grained sandstone samples and might be related to localization of deformation in the central part of the plug in combination with buckling of the sample, whereas the overall deformation of the sample is compaction and porosity reduction. It should also be kept in mind that the local strain sensors are getting close to their range limit toward the end of the test. Data from local strain measurements are used throughout the paper.

[24] The axial compression loading tests are compared with the hydrostatic loading path by plotting porosity change and *P* wave velocity change as a function of mean stress for the natural coarse-grained sandstone (Figure 6), the dense fine-grained sand (Figure 7), and the loose fine-grained sand (Figure 8). For all tests, an overall porosity reduction corresponding to *P* wave velocity increase is associated with increasing mean stress, except the 2 MPa test for the dense fine sand (Figure 7). Strain hardening deformation can be characterized as a shear-enhanced compaction, and following *Wong et al*. [1997] and *Fortin et al*. [2005], the onset of shear-enhanced compaction is marked as a point C*, which coincides with the point where the deformation during axial compression deviates from the hydrostatic curve. In our tests, the onset of shear-enhanced compaction is very gradual and the point C* is set as the point where the deformation diverges from the isotropic loading curve for the natural coarse sandstone (Figure 6) and the dense fine sand (Figure 7). Onset of shear-enhanced compaction, C*, and maximum stress conditions for each test is given in Table 3. For the loose fine sand, no interpretation of C* has been marked. The point C* is also marked on the *P* wave velocity plot and found to partly correspond to a change in the velocity trend (Figures 6 and 7). The deformation mode for all the tests is dominated by compaction except for the 2 MPa test for the dense fine sand, where a weak dilation and a peak strength are observed from the curves (Figure 5a). For this test, the peak stress is marked on curves in Figure 7 and is found to correspond to a small reduction in *P* wave velocity. The porosity increase associated with the dilation starts right before peak stress is reached.

6.2. Microstructural Characterization From Posttest Analysis

[25] X-ray CT images together with photomicrographs from thin sections were used to identify deformation mode and grain damage in the tests results. All the tests with tamped sand had three layers of added iron powder, giving a density contrast visible in the X-ray images. These layers were added to help identify the mode of deformation during axial compression. The 3-D reconstruction of the X-ray scans has been inspected by qualitative methods, and a 2-D image

Table 4. Observed Mode of Deformation and Qualitative Description of Cataclasis for the Different Samples

Material	Hydrostatic Loading Pressure (MPa)	Mode of Deformation	Cataclasis
Natural coarse sandstone	40	Compaction	Some
	2	Compaction, no visible localization	Limited, not observed
	5	Compaction, localization of diffuse low-angle bands	Extensive
	15	Compaction, localization of diffuse horizontal bands	Extensive
Fine sand loose	40	Compaction	Some
	2	Compaction and buckling	Limited
	5	Compaction and buckling, possible diffuse localization	Some
Fine sand dense	40	Compaction	Some
	2	Dilation, no visible localization	Limited
	5	Compaction and buckling	Some
	15	Compaction and buckling	Extensive

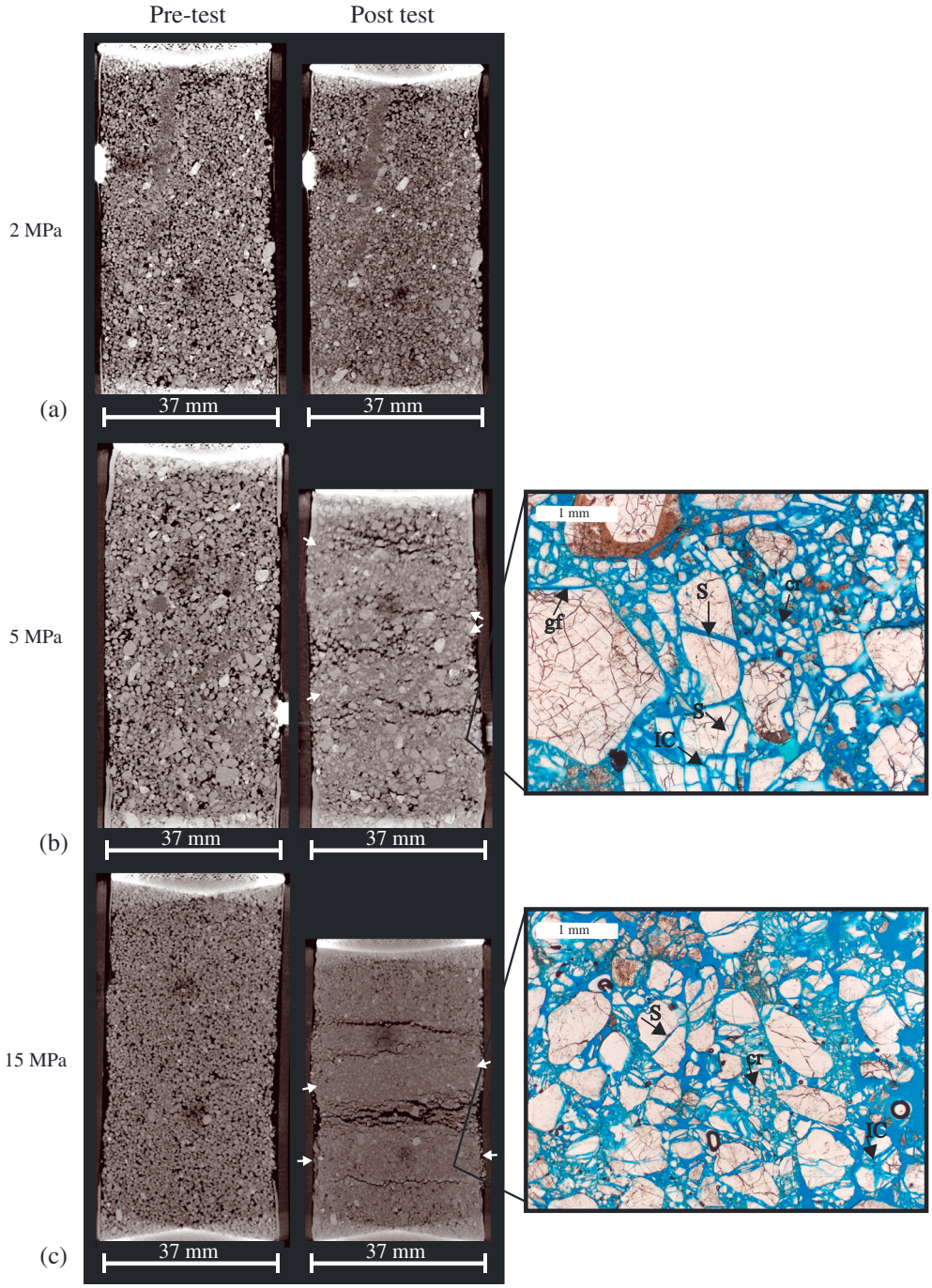

Figure 9. Series of pretest and posttest X-ray images and photomicrographs of natural, coarse-grained sandstone samples deformed at confining pressures of (a) 2, (b) 5, and (c) 15 MPa, respectively. In the X-ray images, black represents open pores and gray are grains, and white arrows indicate zones of localized deformation. Dark fractures might be related to unloading and handling of the deformed sample before scanning. The photomicrographs show different types of grain damage: grain flaking (gf), single fractures (S), irregular complex fractures (IC), and zones with crushed grains (cr). Exact position of the photomicrographs is not known.

is presented that contains the section with the most pronounced deformation. The posttest imaging was performed after the unloading of the sample and used for a qualitative description of deformation mechanisms that can be observed. A summary of the observed deformation mode and grain damage is given in Table 4.

[26] For the natural coarse-grained sandstone sample, pretest and posttest X-ray CT images together with photomicrographs from thin sections are shown in Figure 9. For deformation at a low confining pressure of 2 MPa (Figure 9a), the X-ray image shows an overall compaction of the sample. There are no significant indications of grain crushing in this

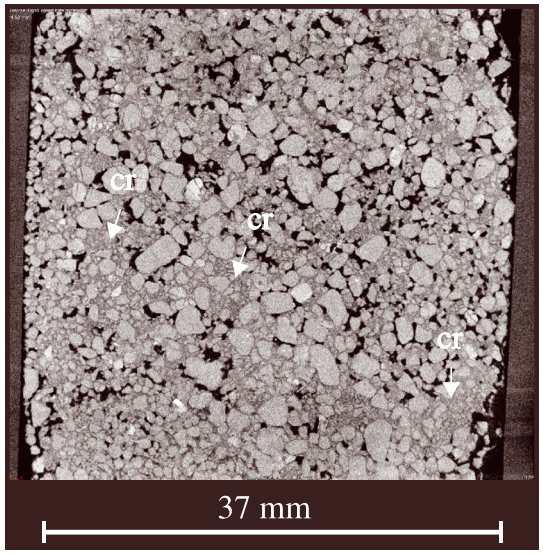

Figure 10. Posttest X-ray CT image from hydrostatic test on natural coarse sandstone. Grain damage can be observed as zones with grain crushing (cr).

sample, implying that the observed deformation is mainly due to grain rearrangement. A photomicrograph is not available from this test. For deformation at 5 MPa confining pressure (Figure 9b), the X-ray images show overall compaction of the sample. Diffuse low-angle bands with low porosity and extensive grain crushing can be observed and related to localization of deformation. The open fractures are believed to be related to the unloading and handling before the posttest scan. The photomicrograph from the test loaded axially under 5 MPa confining pressure shows extensive grain damage, and various types of grain breakage or damage can be described, such as grain flaking (gf) where deformation is localized to grain edges, single fractures (S) where a grain is split in two, irregular complex fractures (IC) where the grain is split in several parts in a complex pattern, and grain crushing (cr) where the grain is completely crushed into smaller aggregates [*Chuhan et al*., 2002]. The largest compaction and most extensive grain damage are observed in the sample deformed at 15 MPa confining pressure. The compaction was expressed by buckling of the sample membrane and a diffuse horizontal to subhorizontal layering that divided the sample into high-density zones, possibly compaction or shear-enhanced compaction bands, separated by low-density zones that became affected by open fractures related to unloading. The photomicrograph from the 15 MPa confining pressure test (Figure 9c) shows more extensive grain damage than that from the 5 MPa test and is dominated by single fractures (S), irregular complex fractures (IC), and grain crushing (cr). The larger grains in the tested samples sometimes show an irregular pattern of intragrain closed fractures. Such fractures were, however, also found occasionally in undeformed samples (Figure 2) and thus partly relate to the previous (natural) deformation history of this sandstone sample. The grain damage observed for the hydrostatic test (Figure 10) is qualitatively less than the grain damages observed for the 5 MPa confining pressure test.

[27] Posttest X-ray imaging and photomicrographs of the fine-grained sand samples at 2 and 5 MPa confining pressures compare the differences in mode of deformation and fracturing for the loosely and the densely packed samples (Figures 11a–11d). No clear strain localization can be observed for the fine grain sand. For the dense sand, a distinct barrel shape was observed for the test at 2 MPa (Figure 11a), whereas at 5 MPa and for the loose sand, the deformation was dominated by compaction and some buckling (Figures 11b–11d). Based on the photomicrographs, very limited grain fracturing was observed for the tests at 2 MPa (Figures 11a and 11b), whereas for the tests at 5 MPa, grain fracturing and crushing were obvious (Figures 11c and 11d). The amount of grain fracturing in the hydrostatic tests is similar or less than that observed for tests with a 5 MPa confining pressure (Figures 12a and 12b). For the densely packed sand test at 15 MPa, the amount of grain fracturing and grain crushing was more pronounced than for the tests performed with 5 MPa confining pressure (Figure 12c).

7. Discussion

7.1. Variation in Material Properties and Deformation Mechanism

[28] The coarse- and fine-grained materials tested are very different in initial porosity, grain size, and sorting. For the loose and dense fine-grained sand samples, only initial packing and porosity are different. This variation in material properties affects the porosity change and compaction properties of the material. Comparing the results for all tests, the spread in porosity can be observed (Figures 6a, 7a, and 8a and Table 2). The fine-grained sand is found to have a higher initial porosity than the coarse-grained sand that is likely related to its narrow range in grain size distribution (well sorted) (Table 1). The loose packing gives a higher initial porosity than the dense packing for fine-grained sand, but during hydrostatic loading, the loose, most porous sand shows higher porosity reduction than the dense sand.

[29] Various deformation mechanisms like grain fracturing and grain crushing can be observed directly from X-ray CT images and thin section microphotographs (Figures 9–12). The amount of grain damage typically increases with increasing stress (mean and shear stresses) and is also observed to increase slightly with the larger grain size and less well-sorted material. More extensive fracturing in the coarse-grained material compared to the fine-grained material for a similar stress condition is in agreement with findings from *Chuhan et al*. [2002] and *Zhang et al*. [1990a] and possibly related to the smaller number of grain contacts giving higher stress at each contact in a coarse-grained material. The increased fracturing observed can also be related to the higher initial fracture density within the coarse-grained material (Figure 2). The large compaction and porosity reduction observed imply that grain rearrangements, rolling, and slip are important deformation mechanisms that cannot be observed directly. The *P* wave velocity (Figures 6b, 7b, and 8b) was observed to increase during shear-enhanced compaction. This generally indicates compaction and pore collapses as the dominating deformation mechanism, although there is a complex correlation between porosity,

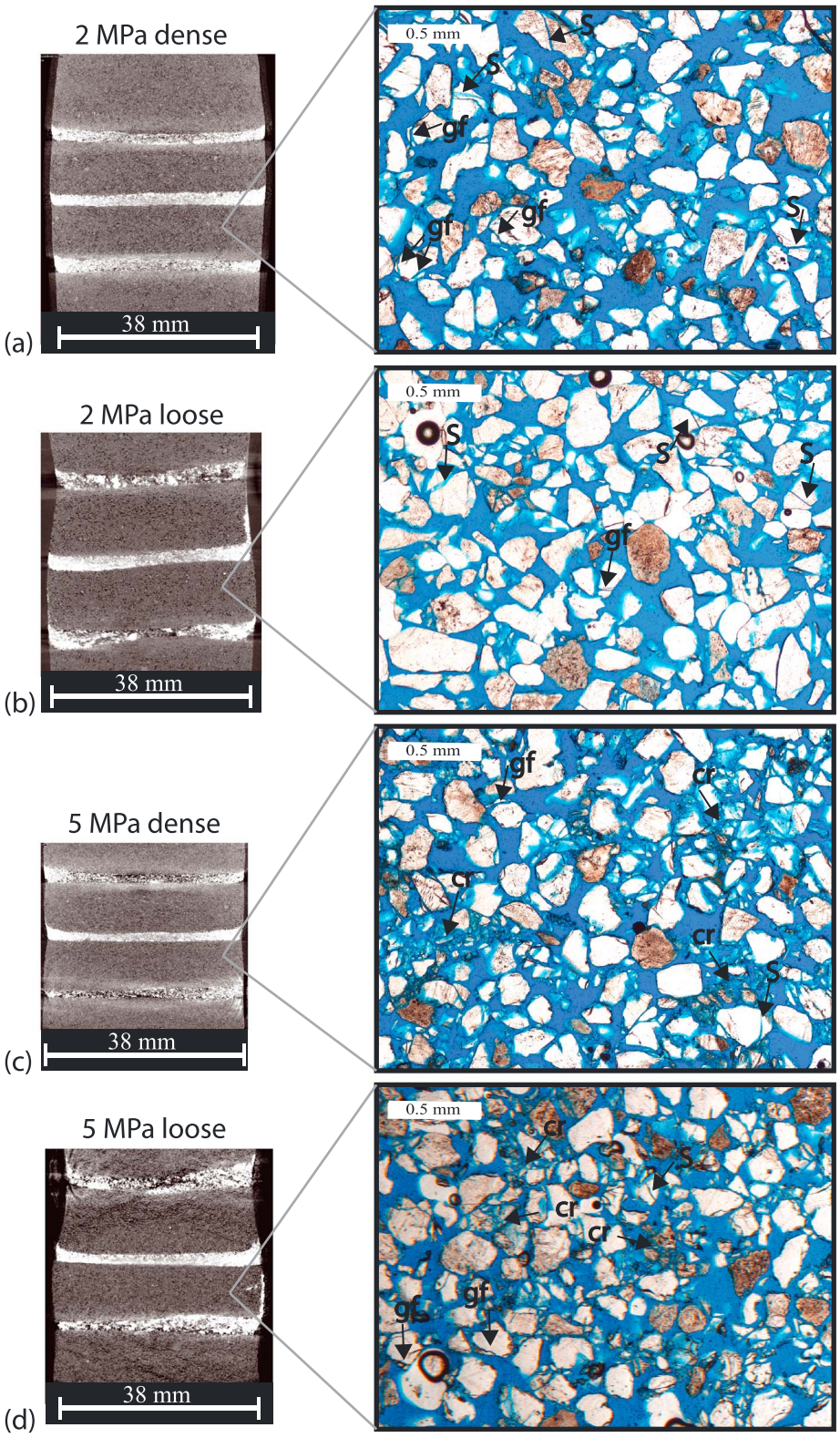

Figure 11. Deformation of loosely and densely packed fine sand (a, b) at 2 MPa confining pressure and (c, d) at 5 MPa. White horizons in the X-ray images are marker horizons added for identification of shear deformation. The photomicrographs display different types of grain damage: grain flaking (gf), single fractures (S), and zones with crushed grains (cr).

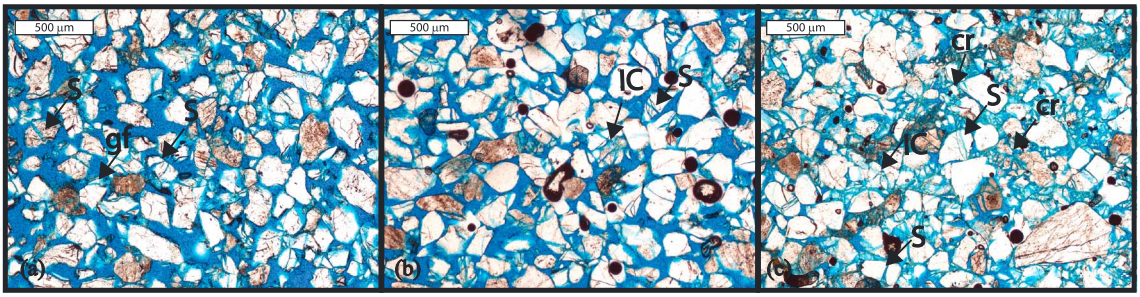

Figure 12. Photomicrographs of observed grain fracturing in (a) hydrostatic tests for the loose fine sand, (b) hydrostatic test on dense fine sand, and (c) dense fine sand deformed at 15 MPa confining pressure. Different types of grain damage such as grain flaking (gf), single fractures (S), and zones with crushed grains (cr) are observed.

fractures, and elastic properties [*Fjaer*, 2006; *Fjaer and Holt*, 1994]. For sandstone, reduction in sonic velocity during axial compression is observed and explained by the nucleation of cracks at the same time as pores are being closed [*Fortin et al*., 2005, 2007]. In the current experiments, grain fracturing and crushing are observed to be important deformation mechanisms, although no reduction in velocity is observed [*Torabi and Skurtveit*, 2013]. *Torabi and Skurtveit* [2013] discuss that static and dynamic M moduli are not in agreement in these experimental results, which is attributed to the fact that M_{dynamic} increases along with porosity reduction (increase in P wave velocity), while M_{static} vanishes possibly due to large strain and grain crushing in the samples.

7.2. Yield Stress and Controlling Parameters for the Yield Cap

[30] The size of the end cap described in the modified Cam-Clay cap model (Figure 1) is defined as the yield stress during hydrostatic loading. In previously reported tests on sandstone, the yield stress, P^*, is marked as a clear yield on the hydrostatic stress-strain curve related to pore collapse [*Fortin et al*., 2005; *Wong et al*., 1997], whereas for the current tests, the yield point is more gradual and difficult to define. The yield stress for a granular material under hydrostatic or uniaxial loading is commonly believed to indicate the onset of marked particle fracturing, splitting, and grain rearrangement [*Chuhan et al*., 2002, 2003; *Mesri and Vardhanabhuti*, 2009; *Nakata et al*., 2001]. This yield stress is normally defined as the point in the void ratio or porosity versus log mean stress curve with the largest curvature (inflection point) for a uniaxial or hydrostatic loading path. The yield stress can be related to the behavior of the tangent constrained modulus (M modulus), where the first reduction in modulus (M_{max}) is believed to mark the onset of grain breakage [*Mesri and Vardhanabhuti*, 2009] and the gradual reduction of M to the second inflection point (M_{min}) reflects the transition from incipient grain crushing (M_{max}) to onset of marked particle damage [*Chuhan et al*., 2003].

[31] Plots of bulk modulus and porosity versus mean stress have been utilized to find the yield points in these experiments (Figures 13a and 13b). The yield points from maximum curvature (MC) are estimated based on the hydrostatic loading paths for the two fine sands and the natural coarse sandstone tested. The tangent bulk modulus K_b, the derivative of the effective confining stress, is computed as a function of strain using equation (3):

$$K_b = \frac{\Delta\sigma'_V + 2\,\Delta\sigma'_H}{3(\,\Delta\varepsilon_V + 2\,\Delta\varepsilon_H)} \tag{3}$$

where $\Delta\sigma'_V$ is the change in effective vertical stress, $\Delta\sigma'_H$ is the change in effective horizontal stress, $\Delta\varepsilon_V$ is the change in vertical strain, and $\Delta\varepsilon_H$ is the change in horizontal strain. Local K_{max} and K_{min} are marked on the curve in Figure 13a for the natural coarse-grained sandstone and the densely packed fine-grained sand. For the loosely packed fine-grained sand, there is no peak but a continuous increase in K with increasing mean stress with a plateau around $p' = 5$ MPa. The break in the bulk modulus curve for the coarse sand was due to a pause in loading, and K_{min} is not reached for the natural coarse sandstone. The mean stress at the maximum curvature yield point is very similar for the dense fine sand and the coarse sand, whereas for the loose sand, the yield is lower (Figure 13b). Yield stress is summarized in Table 5 using both the maximum curvature methods and K_{max}. The ratio between the two values is found to be 0.7 for the coarse-grained sand and 1.3 for the dense fine-grained sand. This ratio is within the same range of 0.7–2.5 given in *Mesri and Vardhanabhuti* [2009]. The results give an estimated yield stress during hydrostatic loading of 12–15 MPa for the natural coarse sandstone and 9–11 MPa for the dense fine-grained sand. For the high-porosity, loose fine-grained sand, the yield stress is less well defined than that for the denser packed sand. The yield stress for granular material is found to vary from 3 to 30 MPa depending on sand characteristics [*Chuhan et al*., 2003], with the lowest yield stress observed when the grain size is large, grains are angular, grain strength is low, or the material is well sorted.

[32] The inflection point of the hydrostatic curve for sandstone is believed to correspond to the critical effective pressure for onset of grain crushing based on microscopic observations of Hertzian fractures [*Zhang et al*., 1990a] and is further constrained by simultaneous measurements of confining pressure, pore pressure, porosity change, and acoustic emission by *Zhang et al*. [1990b]. Based on the findings of *Zhang et al*. [1990a], a correlation between

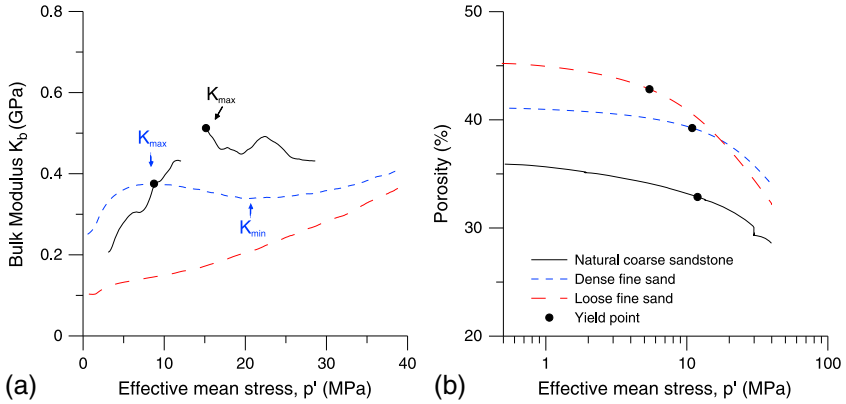

Figure 13. (a) Yield points interpreted from bulk modulus and (b) maximum curvature of the porosity for hydrostatic test for natural coarse sandstone, loose fine sand, and dense fine sand. Color codes for the curves are found in the inset legend. Break in the curve for natural coarse-grained sandstone is due to pause in loading.

porosity and grain size and the onset of pore collapse and Hertzian fracturing in hydrostatic tests is used to empirically predict the onset of grain crushing or pore collapse pressure:

$$P^* \propto (\varphi\, R)^n \tag{4}$$

where φ is the porosity, R is the grain radius, and $n \approx -3/2$. This relationship is found to hold for the tests described in *Wong et al.* [1997]. Comparing the results found from this relationship with the yield stress from our hydrostatic tests on noncemented sand shows that the natural coarse-grained sandstone sample shows a reasonable fit, whereas the fine-grained sand tamped in the laboratory gives a lower yield stress than that predicted by the relationship in equation (4) (Figure 14). Similarly, the yield stress for sands tested by *Crawford et al.* [2004] was also lower than predicted using the relationship in *Zhang et al.* [1990a]. *Crawford et al.* [2004] found that the yield cap was better related to the preconsolidation pressure used for some of the sands tested. Observations from stress cycling experiments on granular quartz sand show deformation similar to yielding when loading exceeds the previous loading stage, indicating that the granular material retains memory of the previous loading stage [*Karner et al.*, 2003]. This suggests that the measured yield stress could be related to the maximum burial depth. In the test series presented in this paper, no preconsolidation pressure is imposed on the sample during testing. On the other side, the natural coarse sandstone is tested with its natural packing that has experienced a maximum burial of 400 ± 100 m [*Ballas et al.*, 2013]. The hydrostatic yield stress of 12–15 MPa observed for the natural coarse-grained sample is found to be in the same range as the yield stress estimated using the relationship described by *Zhang et al.* [1990a] but can also be related to its intact and natural packing inherited from its burial history.

[33] For the fine-grained sand, a hydrostatic yield is observed for the densely packed sand, whereas for the loosely packed sand, the yield is less pronounced, suggesting that the yield stress is partly controlled by the porosity related to initial packing of the material. The initial density of the sample is related to tamping of the sample during sample preparation and may be considered as a similar process as preconsolidation of the sample. The yield stress observed for the fine-grained sand (10 MPa) is significantly lower than the estimated yield due to pore collapse (around 100 MPa). Posttest photomicrograph of the hydrostatic loading tests on fine-grained sand (Figures 12a and 12b) shows limited grain crushing, suggesting that the dominating deformation mechanism during yield is grain rearrangement and slip, with only minor grain fracturing. For the natural coarse-grained sandstone, the posttest X-ray image (Figure 10) indicates more extensive grain crushing. The lower yield stress observed for the tests on noncemented sand can thus be explained by the dominating deformation mechanism being grain rearrangement and slip for the porous fine-grained sand related to the packing density. Deformation of less porous coarse-grained sandstone is also controlled by the onset of grain crushing possibly due to its initial grain size and sorting. Other parameters like the rate of deformation are also found to significantly influence the end cap, where higher strain rate typically corresponds to higher yield stress [*Hagin and Zoback*, 2004]. This effect has not been investigated during this experimental work; the same strain rate is used for all the tests.

7.3. Shear-Enhanced Compaction

[34] Onset of shear-enhanced compaction, C*, has been successfully described for porous sandstones using end cap models and yield stress related to the pore collapse [*Wong and Baud*, 2012]. However, for noncemented, poorly lithified sandstone and sand, variation in consolidation

Table 5. Yield Stress p' for the Three Materials Using Maximum Curvature MC and Bulk Modulus K_{max}

Material	$p'\,K_{max}$ (MPa)	p' MC (MPa)	p' MC/$p'\,K_{max}$
Natural coarse sandstone	15.2	11.9	0.7
Loose fine sand	-	5.4	-
Dense fine sand	8.7	10.9	1.3

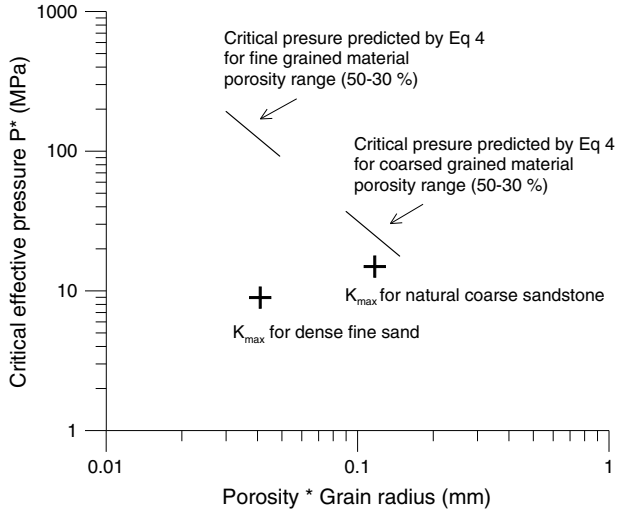

Figure 14. Comparing the relationship between porosity × grain size and critical pressure for onset of grain crushing using equation (4) [*Zhang et al*., 1990a] and the K_{max} yield points found from the hydrostatic tests in this work.

pressure is associated with large inelastic deformation. The combined effect of elastic and inelastic deformation observed during compaction of the noncemented sand tested here is expressed as porosity reduction during both the hydrostatic loading and axial compression. Due to this large change in porosity, shear-enhanced compaction for various consolidation pressures cannot be described by one single end cap. Rather, end caps for different porosities during hydrostatic loading can be used to describe the change in porosity during shear-enhanced compaction. Expending yield caps with increasing porosity is also described by *Wong et al*. [1992].

[35] In our tests, elliptical end caps are calculated using equation (1) for effective pressure p' found for various porosities in the hydrostatic tests. The calculated end cap is then compared with the measured porosity during shear-enhanced compaction in tests with axial loading using *p-q* plots (Figures 15a, 16a, and 17a). End caps for given porosities and the critical state line are mapped in the *p-q* plot together with stress paths and stress condition for selected porosities during axial loading. The critical state line was calculated from equation (2) using a friction coefficient of $\varphi = 32.5$ for the coarse-grained sandstone, $\varphi = 34$ for the dense fine-grained sand, and $\varphi = 28$ for the loose fine-grained sand. The friction coefficient is determined using the maximum shear strength, τ, from tests where close to constant differential stress is reached at the end of test (Figure 5).

[36] Porosity values for the interpreted yield stress based on K_{max} in the hydrostatic curves (Table 5) and the yield stress for onset of shear-enhanced compaction, C*, (Table 3), during axial compression interpreted for the natural coarse sandstone and the dense fine sand are added in the *p-q* plot (Figures 15a and 16a). For the loosely packed fine-grained sand, no yield stress is defined; instead, the stress conditions for selected porosities along the axial compression stress path are plotted (Figure 17a). Porosity loss during shear-enhanced compaction gives a reasonable fit with predicted end caps from porosity loss during hydrostatic loading. The best fit with the end cap model is found for the fine-grained sand samples tamped in the laboratory, whereas for the coarse-grained sand, the results are a bit more scattered due to the natural variability in the initial porosity of these samples. These porosity contour lines show end caps demonstrating porosity loss at shear stresses lower than what is need to reach the failure line (the critical state line). The yield stress marked as onset of shear-enhanced compaction, C*, is not found to map out a single end cap as observed for sandstone [*Wong and Baud*, 2012] but relates to the observed porosity reduction.

[37] The mode of deformation observed in the tests is illustrated by the stress-strain curve for the axial compression tests (Figures 15b, 16b, and 17b) and shows that for the natural, coarse-grained sandstone and the densely packed sand, the yield was dominated by compaction for high confining pressures and with increasing shear during failure at lower confining pressures. The greater shear component

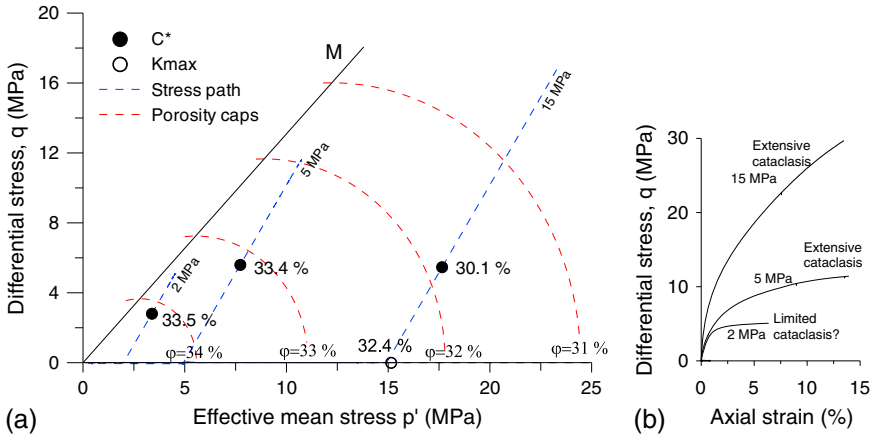

Figure 15. (a) Shear-enhanced compaction, C*, from axial compression tests on natural coarse sandstone samples compared with critical state line, M, and yield caps calculated for given changes in porosity during hydrostatic loading. (b) Stress-strain curve for the 2, 5, and 15 MPa stress paths showing the variation in deformation mode and qualitative description of observed cataclasis.

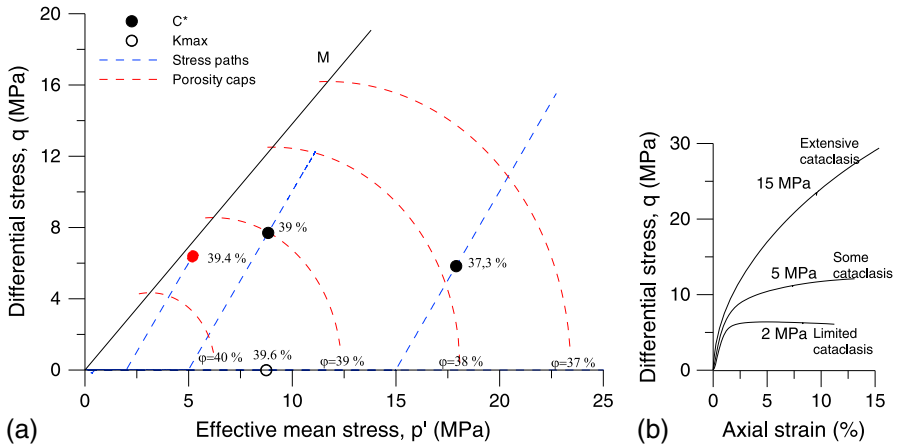

Figure 16. (a) Shear-enhanced compaction, C*, from axial compression tests on dense fine sand compared with critical state line, M, and yield caps calculated for given changes in porosity during hydrostatic loading. (b) Stress-strain curve for the 2, 5, and 15 MPa stress paths showing the variation in deformation mode and qualitative description of observed cataclasis.

during yielding at low confining pressure corresponds to yielding closer to the failure line, whereas at high confining pressure, the deformation is dominated by compaction with less shear localization. The 2 MPa test for the dense fine sand yields with a slight dilation and barrel shape after reaching close to the failure line, but no significant softening is observed. The change in deformation mode from compaction- to shear-dominated deformation with decreasing confining stress corresponds to previous observations reported for cemented sandstone [*Baud et al.*, 2004; *Fortin et al.*, 2005]. The fine-grained sand with the looser initial packing (highest porosity) was dominated by compaction and strain hardening, demonstrating that the mode of deformation (shear versus compaction) depends on the porosity related to the packing configuration in addition to the confining stress and distance from the critical state line. The denser packed sand is stiffer with a pronounced yield, whereas the loose packed sand is dominated by compaction and strain hardening with no marked yield stress during axial compression for similar confining stress. The most pronounced localization of deformation is observed for the natural coarse-grained, low-porosity sandstone (Figure 9) where grain crushing is most prominent. Both the fine-grained and the coarse-grained materials deform by a combination of the different deformation mechanisms, and more detailed experimental work is suggested to better define the stress conditions for transition in deformation mechanism controlling the yield stress for shallow burial conditions.

7.4. Implication for Reservoir Quality

[38] The application of this study is to better understand the deformation mechanism and formation of deformation bands in noncemented and poorly lithified sandstone reservoirs. The results show that porosity reduction due to grain rearrangement during compaction and shear-enhanced compaction is an important deformation mechanism together

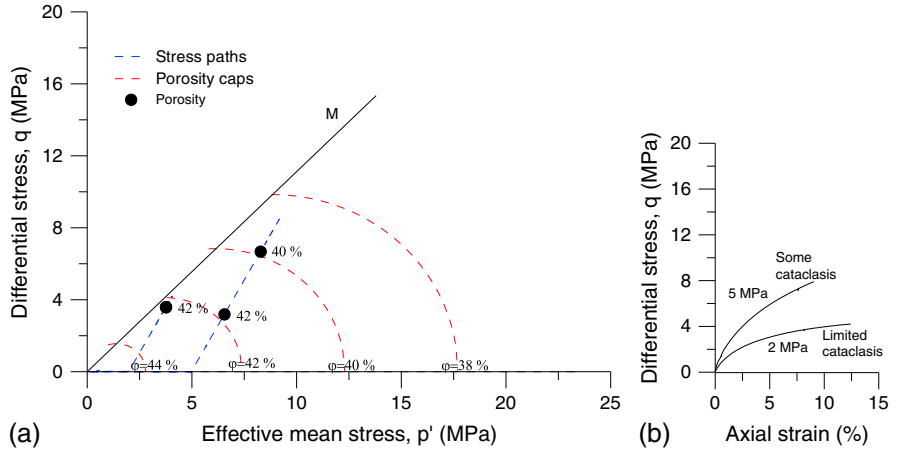

Figure 17. (a) Porosity reduction in axial compression tests on loose fine sand compared with critical state line, M, and yield caps calculated for given changes in porosity during hydrostatic loading. (b) Stress-strain curve for the 2 and 5 MPa stress paths showing the variation in deformation mode and qualitative description of observed cataclasis.

with the gradual onset of grain fracturing. Yield caps can be found for various porosities or packing densities during shear-enhanced compaction, and grain fracturing is observed as an important deformation mechanism for effective pressure conditions as low as 5–10 MPa. This might indicate that compaction structures described in the field as compaction bands [*Mollema and Antonellini*, 1996] and shear-enhanced compaction bands with minor grain comminution [*Ballas et al*., 2013; *Eichhubl et al*., 2010] may form at shallow burial depths in poorly lithified sandstone reservoirs below the yield stress estimated using empirical relationship for sandstones. This is also in agreement with observations of grain fracturing during deformation at the Troll Field at shallow burial conditions [*Gabrielsen and Koestler*, 1987]. Shear-enhanced compaction and localization lower the porosity compared to a near-hydrostatic stress path and hence reduce reservoir quality during tectonic compression. Understanding the mechanism involved in deformation at shallow burial is important when evaluating reservoir properties for CO_2 storage in porous sandstone reservoirs. Compaction and shear-enhanced compaction bands are found to have limited effect on water flow in shallow buried reservoirs in Provence [*Ballas et al*., 2013], whereas the permeability reduction and impact on regional flow are more significant for the more deeply buried Navajo and Aztec Sandstones in the western United States [*Eichhubl et al*., 2004; *Fossen et al*., 2011; *Sun et al*., 2011], where compaction and shear-enhanced compaction bands formed at shallow burial depth with later diagenetic changes influencing the flow properties. In addition, in a reservoir condition, the capillary effect of these deformation bands due to their compaction and grain crushing might influence the sealing capacity of the reservoir [*Torabi et al*., 2013]. This has an important implication for CO_2 storage since capillary trapping is considered as one of the main mechanisms for CO_2 storage underground.

8. Conclusions

[39] In this paper, using an experimental approach, we have studied deformation mechanisms during axial compression of poorly lithified sandstone and sand to increase our understanding of shear-enhanced compaction in shallow reservoir conditions. Samples with different grain sizes, porosities, and packing densities were tested using hydrostatic loading and axial compression. Common characteristics for most of the tests were the large inelastic compaction and porosity reduction during loading. Most tests yield in compaction, showing increasing strain hardening with increasing confining stress. Maximum differential stress seems to be primarily controlled by the confining stress during axial loading, whereas the shape of the stress-strain curve is influenced by the material and initial packing. Increasing *P* wave velocity during loading and yield are signs of compaction that could be due to grain rearrangement and closure of pore space as the dominating deformation mechanism. In addition, microstructural observations demonstrate increasing amount of grain fracturing and grain crushing with increasing stress as the dominant deformation mechanism at high confining pressure. Grain fracturing was also found to be most pronounced for the coarse-grained material. Yield stress during hydrostatic loading is discussed using methodologies from soil mechanics and found to be lower than predicted using empirical relationships for estimating yield stress related to pore collapse in well-lithified and cemented sandstone. Furthermore, yield during shear-enhanced compaction is compared with a modified Cam-Clay cap model. Porosity loss during shear-enhanced compaction gives a reasonable fit with end caps calculated from porosity loss during hydrostatic loading and demonstrates how end caps change during compaction and increasing confining pressure for the different types of material tested. Deformation is dominated by strain hardening and compaction with increasing shear deformation for tests yielded close to the failure line in the *p-q* diagram. The deformation mechanism is also found to vary depending on the porosity and type of material. Two different deformation mechanisms are observed for the tests: (1) grain rearrangement, rolling, and slip; and (2) grain damage, such as fracturing, splitting, and crushing. At low stress, grain rearrangement is dominating, primarily controlled by the porosity and interparticle friction [*Mesri and Vardhanabhuti*, 2009], whereas the onset of grain damage is controlled by the stress and material properties like mineralogy and grain size [*Chuhan et al*., 2002]. The combined insight from the tests and microstructural observations presented suggests that the hydrostatic yield strength observed for the fine-grained and very porous sand was primarily controlled by the packing density with deformation dominated by grain rearrangement. For the coarse-grained sandstone with lower porosity due to poor sorting, it is suggested that the hydrostatic yield strength and localization observed during shear-enhanced compaction above 5 MPa confining stress are related to the onset of grain fracturing. This observed onset of grain fracturing at an effective pressure of 5–10 MPa supports the idea that cataclastic shear-enhanced compaction bands might have been formed at a shallow burial depth in the field.

[40] **Acknowledgments.** We would like to thank T. Berre, M. Soldal, and the technical staff at the Norwegian Geotechnical Institute (NGI) for assistance during the experimental work and G. Ballas at the University of Montpellier 2 for discussions, comments, and assistance during sampling of material. H. Fossen, J. Rudnicki, A. Kohli, and P. Ringrose are thanked for their comments to the manuscript. Thanks also to P. Eichhubl and one anonymous reviewer for helpful suggestions and improvements. This study is part of a consortium R&D project 207806, the IMPACT Project, funded by the CLIMIT Program at the Research Council of Norway and Statoil.

References

Antonellini, M. A., A. Aydin, and D. D. Pollard (1994), Microstructure of deformation bands in porous sandstones at Arches National Park, Utah, *J. Struct. Geol.*, *16*(7), 941–959.

Aydin, A., and A. M. Johnson (1983), Analysis of faulting in porous sandstones, *J. Struct. Geol.*, *5*(1), 19–31.

Aydin, A., R. I. Borja, and P. Eichhubl (2006), Geological and mathematical framework for failure modes in granular rock, *J. Struct. Geol.*, *28*(1), 83–98.

Ballas, G., R. Soliva, J. P. Sizun, A. Benedict, T. Cavailhes, and S. Raynaud (2012), The importance of the degree of cataclasis in shear bands for fluid flow in porous sandstone, Provence, France, *AAPG Bull.*, *96*(11), 2167–2186.

Ballas, G., R. Soliva, J.-P. Sizun, H. Fossen, A. Benedicto, and E. Skurtveit (2013), Shear-enhanced compaction bands formed at shallow burial conditions; implications for fluid flow (Provence, France), *J. Struct. Geol.*, *47*(0), 3–15.

Balsamo, F., and F. Storti (2010), Grain size and permeability evolution of soft-sediment extensional sub-seismic and seismic fault zones in high-porosity sediments from the Crotone basin, southern Apennines, Italy, *Mar. Pet. Geol.*, *27*(4), 822–837.

Balsamo, F., and F. Storti (2011), Size-dependent comminution, tectonic mixing, and sealing behavior of a "structurally oversimplified" fault zone in poorly lithified sands: Evidence for a coseismic rupture?, *Geol. Soc. Am. Bull.*, *123*(3–4), 601–619.

Baud, P., E. Klein, and T. F. Wong (2004), Compaction localization in porous sandstones: Spatial evolution of damage and acoustic emission activity, *J. Struct. Geol.*, *26*(4), 603–624.

Berre, T. (2011), Triaxial testing of soft rocks, *Geotech. Test. J.*, *34*(1), 61–75.

Bésuelle, P., and J. W. Rudnicki (2003), Localization: Shear bands and compaction bands, in *International Geophysics*, edited by G. Yves and B. Maurice, chap. 5, pp. 219–321, Academic Press, London.

Bésuelle, P., J. Desrues, and S. Raynaud (2000), Experimental characterisation of the localisation phenomenon inside a Vosges sandstone in a triaxial cell, *Int. J. Rock Mech. Min. Sci.*, *37*(8), 1223–1237.

Cashman, S., and K. Cashman (2000), Cataclasis and deformation-band formation in unconsolidated marine terrace sand, Humboldt County, California, *Geology*, *28*(2), 111–114.

Cheung, C. S., P. Baud, and T. F. Wong (2012), Effect of grain size distribution on the development of compaction localization in porous sandstone, *Geophys. Res. Lett.*, *39*, L21302, doi:10.1029/2012GL053739.

Chuhan, F. A., A. Kjeldstad, K. Bjørlykke, and K. Høeg (2002), Porosity loss in sand by grain crushing—Experimental evidence and relevance to reservoir quality, *Mar. Pet. Geol.*, *19*(1), 39–53.

Chuhan, F. A., A. Kjeldstad, K. Bjorlykke, and K. Hoeg (2003), Experimental compression of loose sands: Relevance to porosity reduction during burial in sedimentary basins, *Can. Geotech. J.*, *40*(5), 995–1011.

Crawford, B., M. Gooch, and D. Webb (2004), Textural controls on constitutive behavior on unconsolidated sands: Micromechanics and cap plasticity, 6th, ARMA/NARMS Rock Mechanics Across Borders and Disciplines GULF ROCKS.

Cuisiat, F., and E. Skurtveit (2010), An experimental investigation of the development and permeability of clay smears along faults in uncemented sediments, *J. Struct. Geol.*, *32*(11), 1850–1863.

Cuisiat, F., H. P. Jostad, L. Andresen, E. Skurtveit, E. Skomedal, M. Hettema, and K. Lyslo (2010), Geomechanical integrity of sealing faults during depressurisation of the Statfjord Field, *J. Struct. Geol.*, *32*(11), 1754–1767.

Desrues, J., and G. Viggiani (2004), Strain localization in sand: An overview of the experimental results obtained in Grenoble using stereophotogrammetry, *Int. J. Numer. Anal. Methods Geomech.*, *28*(4), 279–321.

Du BernardX., P. Labaume, C. Darcel, P. Davy, and O. Bour (2002), Cataclastic slip band distribution in normal fault damage zones, Nubian sandstones, Suez rift, *J. Geophys. Res.*, *107*(B7), 2141, doi:10.1029/2001JB000493.

Eichhubl, P., W. L. Taylor, D. D. Pollard, and A. Aydin (2004), Paleo-fluid flow and deformation in the Aztec Sandstone at the Valley of Fire, Nevada—Evidence for the coupling of hydrogeologic, diagenetic, and tectonic processes, *Geol. Soc. Am. Bull.*, *116*(9–10), 1120–1136.

Eichhubl, P., J. N. Hooker, and S. E. Laubach (2010), Pure and shear-enhanced compaction bands in Aztec Sandstone, *J. Struct. Geol.*, *32*(12), 1873–1886.

Fisher, Q., and R. Knipe (2001), The permeability of faults within siliciclastic petroleum reservoirs of the North Sea and Norwegian Continental Shelf, *Mar. Pet. Geol.*, *18*(10), 1063–1081.

Fjaer, E. (2006), Modeling the stress dependence of elastic wave velocities in soft rocks, paper presented at Golden Rocks 2006, The 41st US Symposium on Rock Mechanics (USRMS).

Fjaer, E., and R. M. Holt (1994), Rock acoustics and rock mechanics: Their link in petroleum engineering, *Leading Edge*, *13*(4), 255–258.

Fortin, J., A. Schubnel, and Y. Gueguen (2005), Elastic wave velocities and permeability evolution during compaction of Bleurswiller sandstone, *Int. J. Rock Mech. Min. Sci.*, *42*(7–8), 873–889.

Fortin, J., Y. Guéguen, and A. Schubnel (2007), Effects of pore collapse and grain crushing on ultrasonic velocities and Vp/Vs, *J. Geophys. Res.*, *112*, B08207, doi:10.1029/2005JB004005.

Fossen, H. (2010), Deformation bands formed during soft-sediment deformation: Observations from SE Utah, *Mar. Pet. Geol.*, *27*(1), 215–222.

Fossen, H., R. A. Schultz, Z. K. Shipton, and K. Mair (2007), Deformation bands in sandstone: A review, *J. Geol. Soc. London*, *164*, 755–769.

Fossen, H., R. A. Schultz, and A. Torabi (2011), Conditions and implications for compaction band formation in the Navajo Sandstone, Utah, *J. Struct. Geol.*, *33*(10), 1477–1490.

Gabrielsen, R., and A. G. Koestler (1987), Description and structural implications of fractures in late Jurassic sandstones of the Troll Field, northern North Sea, *Nor. Geol. Tidsskr.*, *67*(4), 371–381.

Hagin, P., and M. Zoback (2004), Viscoplastic deformation in unconsolidated reservoir sands (Part 1): Laboratory observations and time-dependent end cap models, SPE/ARMS, 04–567.

Hall, S. A., M. Bornert, J. Desrues, Y. Pannier, N. Lenoir, G. Viggiani, and P. Besuelle (2010), Discrete and continuum analysis of localised deformation in sand using X-ray μCT and volumetric digital image correlation, *Geotechnique*, *60*(5), 315–322.

Karner, S. L., F. M. Chester, A. K. Kronenberg, and J. S. Chester (2003), Subcritical compaction and yielding of granular quartz sand, *Tectonophysics*, *377*(3), 357–381.

Karner, S. L., A. K. Kronenberg, F. M. Chester, J. S. Chester, and A. Hajash (2008), Hydrothermal deformation of granular quartz sand, *J. Geophys. Res.*, *113*, B05404, doi:10.1029/2006JB004710.

Ladd, R. (1978), Preparing test specimens using undercompaction, *ASTM Geotech. Test. J.*, *1*(1), doi:10.1520/GTJ10364J.

Lothe, A. E., R. H. Gabrielsen, N. B. Hagen, and B. T. Larsen (2002), An experimental study of the texture of deformation bands: Effects on the porosity and permeability of sandstones, *Pet. Geosci.*, *8*(3), 195–207.

Mair, K., I. Main, and S. Elphick (2000), Sequential growth of deformation bands in the laboratory, *J. Struct. Geol.*, *22*(1), 25–42.

Mesri, G., and B. Vardhanabhuti (2009), Compression of granular materials, *Can. Geotech. J.*, *46*(4), 369–392.

Mollema, P. N., and M. A. Antonellini (1996), Compaction bands: A structural analog for anti-mode I cracks in aeolian sandstone, *Tectonophysics*, *267*(1–4), 209–228.

Mondol, N. H., K. Bjorlykke, and J. Jahren (2008), Experimental compaction of clays: Relationship between permeability and petrophysical properties in mudstones, *Pet. Geosci.*, *14*(4), 319–337.

Nakata, Y., M. Hyodo, A. F. L. Hyde, Y. Kato, and H. Murata (2001), Microscopic particle crushing of sand subjected to high pressure one-dimensional compression, *Soils Found.*, *41*(1), 69–82.

Olsson, W. A. (1999), Theoretical and experimental investigation of compaction bands in porous rock, *J. Geophys. Res.*, *104*(B4), 7219–7228.

Rudnicki, J. W., and J. R. Rice (1975), Conditions for localization of deformation in pressure-sensitive dilatant materials, *J. Mech. Phys. Solids*, *23*(6), 371–394.

Rykkelid, E., and E. Skurtveit (2008), Experimental work on unconsolidated sand: The effect of burial depth at time of deformation, paper presented at The 42nd US Rock Mechanics Symposium (USRMS).

Schultz, R. A. (2009), Scaling and paleodepth of compaction bands, Nevada and Utah, *J. Geophys. Res.,*, *114*, B03407, doi:10.1029/2008JB005876.

Schultz, R. A., and R. Siddharthan (2005), A general framework for the occurrence and faulting of deformation bands in porous granular rocks, *Tectonophysics*, *411*(1–4), 1–18.

Skurtveit, E., A. Torabi, R. H. Gabrielsen, R. Alikarami, G. Ballas, H. Fossen, and R. Soliva (2012), Deformation mechanisms in uncemented sandstone, examples from triaxial tests, paper presented at EAGE Fault and Top Seals, EAGE, Montpellier, France.

Soliva, R., R. A. Schultz, G. Ballas, A. Taboada, C. Wibberley, E. Saillet, and A. Benedicto (2013), A model of strain localization in porous sandstone as a function of tectonic setting, burial and material properties; new insight from Provence (southern France), *J. Struct. Geol.*, *49*, 50–63.

Solum, J. G., J. Brandenburg, S. J. Naruk, O. V. Kostenko, S. J. Wilkins, and R. A. Schultz (2010), Characterization of deformation bands associated with normal and reverse stress states in the Navajo Sandstone, Utah, *AAPG Bull.*, *94*(9), 1453–1475.

Sternlof, K. R., J. R. Chapin, D. D. Pollard, and L. J. Durlofsky (2004), Permeability effects of deformation band arrays in sandstone, *AAPG Bull.*, *88*(9), 1315–1329.

Sun, W. C., J. E. Andrade, J. W. Rudnicki, and P. Eichhubl (2011), Connecting microstructural attributes and permeability from 3-D tomographic images of in situ shear-enhanced compaction bands using multiscale computations, *Geophys. Res. Lett.*, *38*, L10302, doi:10.1029/2011GL047683.

Tembe, S., P. Baud, and T. F. Wong (2008), Stress conditions for the propagation of discrete compaction bands in porous sandstone, *J. Geophys. Res.*, *113*, B09409, doi:10.1029/2007JB005439.

Torabi, A. (2012), Deformation of poorly consolidated sandstone in Aghione Formation, Corisca, France., paper presented at EAGE Fault and Top Seals, EAGE, Montpellier, France.

Torabi, A., and E. Skurtveit (2013), Effect of initial grain size and packing on the evolution of elastic properties of poorly lithified sandstones, paper presented at 47th US Rock Mechanics/Geomechanics Symposium, San Fransisco, 23–26 June.

Torabi, A., A. Braathen, F. Cuisiat, and H. Fossen (2007), Shear zones in porous sand: Insights from ring-shear experiments and naturally deformed sandstones, *Tectonophysics*, *437*(1–4), 37–50.

Torabi, A., H. Fossen, and A. Braathen (2013), Insight into petrophysical properties of deformed sandstone reservoirs, *AAPG Bull.*, *20*, 130–218.

Underhill, J. R., and N. H. Woodcock (1987), Faulting mechanisms in high-porosity sandstones; New Red Sandstone, Arran, Scotland, *Geol. Soc., London Spec. Publ.*, *29*(1), 91–105.

Wang, Z., and L. J. Gelius (2010), Electric and elastic properties of rock samples: A unified measurement approach, *Pet. Geosci.*, *16*(2), 171–183.

Wibberley, C. A. J., J.-P. Petit, and T. Rives (2007), The mechanics of fault distribution and localization in high-porosity sands, Provence, France, *Geol. Soc., London Spec. Publ.*, *289*(1), 19–46.

Wong, T. F., and P. Baud (2012), The brittle-ductile transition in porous rock: A review, *J. Struct. Geol.*, *44*, 25–53.

Wong, T. F., H. Szeto, and J. Zhang (1992), Effect of loading path and porosity on the failure mode of porous rocks, *Appl. Mech. Rev.*, 45(8), 281–293.

Wong, T. F., C. David, and W. L. Zhu (1997), The transition from brittle faulting to cataclastic flow in porous sandstones: Mechanical deformation, *J. Geophys. Res.*, *102*(B2), 3009–3025.

Zhang, J. X., T. F. Wong, and D. M. Davis (1990a), Micromechanics of pressure-induced grain crushing in porous rocks, *J. Geophys. Res.*, *95*(B1), 341–352.

Zhang, J. X., T. F. Wong, T. Yanagidani, and D. M. Davis (1990b), Pressure-induced microcracking and grain crushing in Berea and Boise sandstones: Acoustic emission and quantitative microscopy measurements, *Mech. Mater.*, *9*(1), 1–15.

Zoback, M. D., and J. D. Byerlee (1976), Effect of high-pressure deformation on permeability of Ottawa sand, *AAPG Bull.*, *60*(9), 1531–1542.